BIOCHEMISTRY
including biophysical chemistry & molecular biology
Article

Biochemistry **2009,** *48,* 6441–6449 6441
DOI: 10.1021/bi900682w

Structurally Distinct Amyloid Protofibrils Form on Separate Pathways of Aggregation of a Small Protein†

Santosh Kumar and Jayant B. Udgaonkar*

National Centre for Biological Sciences, Tata Institute of Fundamental Research, Bangalore 560 065, India

Received April 21, 2009; Revised Manuscript Received June 4, 2009

ABSTRACT: Understanding the structural as well as mechanistic basis of the conformational polymorphism evident during amyloid protofibril and fibril formation by proteins is an important goal in the study of protein aggregation. In this report, we compare two separate routes to amyloid protofibril formation by the small protein barstar, one induced by the addition of trifluoroethanol (TFE) and the other by heat. The study reveals that the TFE-induced aggregation of barstar leads to protofibrils that differ from heat-induced protofibrils in their external dimensions and internal structures as well as in the mechanisms of their formation. Atomic force microscopy reveals that the TFE-induced protofibrils have about half the thickness of the heat-induced protofibrils. The thickness of the TFE-induced protofibrils (1.14 ± 0.24) suggests that they form a β-sheet monolayer, while the thickness of the heat-induced protofibrils (2.56 ± 0.32) suggests that they are built up from a pair (bilayer) of β-sheets. Fourier-transform infrared (FTIR) as well as circular dichroism (CD) spectroscopy shows that the heat-induced protofibrils are not pure β-sheet structures but that they also contain other structures (α-helix and/or random coil). In contrast, the TFE-induced protofibrils contain more β-sheet structures and less of other structures, if any. The FTIR and CD spectra also reveal that the two differently created protofibrils differ in the internal structures of their β-sheets. The TFE-induced protofibrils differ from the heat-induced protofibrils also in the kinetics of their formation. For the heat-induced reaction, the kinetics are monophasic without any lag phase, while the kinetics of the formation of TFE-induced protofibrils are sigmoidal with an initial lag phase. It appears that the TFE-induced and the heat-induced reactions involve distinct pathways for the formation of amyloid protofibrils. The existence of alternative pathways leading to amyloid protofibrils of distinct structures has important implications in understanding the kinetic origin of amyloid polymorphism.

Amyloid fibrils are long, relatively straight, unbranched nanostructures that nearly any protein can self-assemble into (*1*). The cross-β motif (*2*, *3*), in which the β-strands are oriented perpendicular to and β-sheets are oriented parallel to the fibril axis, appears to be a common feature of all amyloid fibrils, suggesting that proteins may share a common mechanism of fibril formation (*4*). But the exact molecular structure of the cross-β motif can show variations (*5*). The same protein can form amyloid fibrils of multiple distinct conformations, not only in response to a change in the fibril growth conditions (*6*−*8*) or the primary amino acid sequence of the protein (*9*) but even under a single growth condition (*10*, *11*). Multiple conformational variants may differ in the number of protofilaments that comprise the mature fibrils (*11*, *12*) and in the helicity of their intertwining (*10*, *11*), as well as in their underlying molecular structures (*6*, *13*).

The heterogeneity seen in amyloid fibril structure appears to originate during the fibrillation process itself. For some proteins, amyloid fibril formation appears to be nucleation-dependent (*14*): the formation of a critical nucleus acts as the rate-determining step in the overall process. In such cases, amyloid fibrils appear to grow by monomer addition, and no oligomeric and protofibrillar intermediates appear to be formed (*15*, *16*). For many other proteins, however, spherical oligomers as well as elongated, worm-like protofibrils are seen to form rapidly (*17*−*25*) and are the predominant species early during amyloid fibril formation; mature amyloid fibrils appear only later during the process. In such cases, amyloid fibril formation might nucleate by conformational changes in the oligomeric and/or protofibrillar intermediates, and many possible fibril nucleation and growth mechanisms might exist. Alternative nucleation and growth mechanisms may underlie the polymorphism seen in the amyloid fibrils (*8*−*10*). The oligomeric as well as protofibrillar structures are themselves heterogeneous (*25*); consequently, amyloid fibril polymorphism may arise as a consequence of this heterogeneity. Hence, it has become important to understand the structures of protofibrils. But very little is known about the internal structures

†This work was funded by the Tata Institute of Fundamental Research, Government of India. S.K. is the recipient of a Senior Research Fellowship from the CSIR, Government of India. J.B.U. is the recipient of a JC Bose National Fellowship from the Government of India.

*Corresponding author. E-mail: jayant@ncbs.res.in. Phone: 91-80-23666152. Fax: 91-80-23636462.

Published on Web 06/08/2009

of protofibrils, although it appears that the β-sheet elements comprising the amyloid fibril are already present in protofibrils, at least in the case of the amyloid-β protein (*26*).

The necessity of understanding the conformational heterogeneity inherent in the aggregation process (*27*) is highlighted by the phenomenon of prion strains (*28*), wherein infectious particles formed from the same prion protein lead to phenotypically distinct transmissible states. The same prion protein can adopt a range of infectious conformations which differ in their specificity and transmission barrier (*29*−*31*). Obtaining an insight into the structural as well as mechanistic basis of amyloid polymorphism has critical implications for understanding the phenomenon of prion strains. In this context, investigating the effect of a change in the aggregation conditions on amyloid fibril or protofibril formation becomes important, because different subpopulations of the aggregation-competent intermediates might accumulate under different growth conditions and, thereby, might lead to different amyloid structures.

Barstar is an 89-residue protein, which, like many other proteins, forms soluble oligomers (A form) at low pH. The A form has been extensively characterized. It is shown to be a symmetrical aggregate of 16 monomeric units, and it is molten globule-like in possessing partial secondary structure and a strongly perturbed tertiary structure (*32*−*34*). The A form transforms into amyloid protofibrils and fibrils in a slow process, which is accelerated at higher temperatures (*22*, *23*, *35*). Time-resolved fluorescence studies have suggested that the A form is the direct precursor of the protofibrils (*22*). The protofibrils of barstar appear to be elongated worm-like assemblies of the A form oligomers (*22*, *23*, *25*). The transformation of the A form of barstar into amyloid protofibrils, at higher temperatures, has been shown to occur in a stepwise manner through progressively larger aggregates and alternative pathways (*23*, *25*).

Membranes are known to induce or facilitate protein aggregation reactions, and the mimetic nature of alcohols such as trifluoroethanol (TFE)[1] in this regard is well-known (*36*−*40*). TFE is commonly used as a cosolvent to alter the conformations of proteins and peptides (*41*, *42*) because of its ability to destabilize tertiary structure and induce secondary structure. TFE decreases hydrophobic interactions and enhances polar interactions, and the action of TFE in inducing amyloid fibril formation appears to depend on how it affects the balance between these interactions for any particular protein (*40*). Interestingly, in the case of the amyloid-β protein, the protein aggregates formed in the presence and absence of an organic cosolvent differ in their stabilities as well as in their morphologies (*43*, *44*). It can, therefore, be expected that an organic cosolvent may affect the aggregation reaction by affecting a change in the pathway of aggregation, thereby leading to the production of an aggregate with a different morphology.

In this report, it is shown that the addition of TFE to the A form of barstar leads to the formation of amyloid protofibrils which differ from heat-induced protofibrils in their external dimensions and internal structures as well as in the mechanisms of their formation. Atomic force microscopy (AFM) shows that the two differently created protofibrils have significantly different heights and widths. Fourier-transform infrared spectroscopy (FTIR) as well as far-UV circular dichroism (CD) reveal that the heat-induced protofibrils are not pure β-sheet structures and that they also possess other structures (α-helices and/or random coils). In contrast, the TFE-induced protofibrils are seen to contain relatively more β-structures and less of other structures, if any. Furthermore, FTIR and far-UV CD spectra suggest that the heat-induced and the TFE-induced protofibrils differ in the internal structure of their β-sheets. The TFE-induced protofibrils also differ from the heat-induced protofibrils in the kinetics of their formation. The kinetics of the formation of heat-induced protofibrils are single exponential without any lag phase. In contrast, the kinetics of TFE-induced protofibril formation are sigmoidal with an initial lag phase. It appears that the formation of the structurally distinct protofibrils under these two different growth conditions involves distinct pathways.

EXPERIMENTAL PROCEDURES

Protein Expression and Purification. The expression and purification of wild-type barstar have been described earlier (*32*). The purity of the protein was judged by SDS−PAGE, and by mass spectrometry using a Micromass Q-TOF Ultima spectrometer, to be >98% pure. The mass of the protein, as determined by the mass spectrometry, was 10342 Da.

Buffers, Solutions, and Experimental Conditions. All of the reagents used in this study were of the highest purity grade available from Sigma. All of the buffers contained 1 mM DTT, except those used for CD measurements, which contained 200 μM DTT. The protein concentration was determined by the measurement of absorbance at 280 nm, using $\varepsilon_{280} = 23000\ M^{-1}\ cm^{-1}$. The protein was first dissolved in 20 mM Tris buffer at pH 8 and then was diluted 9-fold into 50 mM Gly buffer at pH 2.68. After an incubation of 2 h at 25 °C, the process of protofibril formation was induced by adding TFE to a final concentration of 10%. The final pH was 2.7. The protein solution was then incubated at 25 °C. Aliquots at different times were withdrawn for the measurements of ThT fluorescence. For the ellipticity at 216 nm (θ_{216nm}) as well as dynamic light scattering measurements, the protein solution, after addition of TFE, was transferred into a cuvette at 25 °C, and the reaction was monitored at different times. Proper care was taken to avoid any variation in temperature, which could occur due to the use of different temperature controlling units. In the case of protofibril formation at 60 °C, the protein stock at pH 8 was diluted 10-fold into 50 mM Gly buffer at pH 2.7. After incubation at 25 °C for 2 h, the solution was heated to 60 °C in a heating block. At different time intervals, aliquots of the solution were withdrawn for doing measurements using the various probes.

For collecting AFM images, FTIR as well as far-UV CD spectra, and for the disaggregation experiments, TFE-induced amyloid protofibrils were formed by incubating 20 μM protein with 10% TFE at pH 2.7, 25 °C, for 45 min, when the process is complete as measured by all of the probes. Heat-induced amyloid protofibrils were formed by heating 20 μM protein at 60 °C, pH 2.7, for 3 h, when the process is complete as measured by all of the probes used (*23*).

Thioflavin T Fluorescence Assay. A calculated amount of protein was added to the thioflavin T-containing 50 mM Tris buffer, such that the final concentrations of protein and dye in the solution were 2 and 10 μM, respectively. The final pH of the solution was 8. Thioflavin T fluorescence was measured on a Fluoromax-3 spectrofluorometer (Jobin Yvon). For the kinetic

[1]Abbreviations: TFE, trifluoroethanol; AFM, atomic force microscopy; FTIR, Fourier-transform infrared; CD, circular dichroism; ThT, thioflavin T; θ_{216nm}, ellipticity at 216 nm; R_H, hydrodynamic radius; SI, scattering intensity; HOI, higher order oligomeric intermediate.

measurements, the sample was excited at 440 nm, and the emission at 482 nm was monitored. The excitation and emission bandwidths were set at 1 and 10 nm, respectively.

Circular Dichroism. Far-UV CD measurements were carried out on a Jasco J-720 spectropolarimeter. The parameters used for measurements of far-UV CD spectra were as follows: step resolution, 1 nm; scan speed, 100 nm/min; and bandwidth, 1 nm. For the kinetic measurements, the ellipticity at 216 nm was monitored.

Dynamic Light Scattering. The dynamic light scattering measurements were carried out using a DynaPro-99 unit (Wyatt Technology Corp.) using the procedure described earlier (*23*). In brief, all of the buffers and the protein solution at pH 8 were filtered using 0.02 μm filters (Whatman Anodisc 13). The scattering intensity at 90° and its autocorrelation were monitored simultaneously after illumination of the sample using a laser at wavelength 829.4 nm. For each kinetic data point, 15 acquisitions were collected, which were resolved into a well-defined Gaussian distribution using DynaLS (Wyatt Technology Corp.). The results of DynaLS analysis were also verified using a Regularization algorithm. The viscosities of the solutions used to calculate the R_H were determined from measurements of the refractive indices. Cumulant analysis (Wyatt Technology Corp.) was used to determine the total scattering intensity.

Atomic Force Microscopy (AFM). The AFM images were acquired on a PicoPlus AFM instrument (Molecular Imaging Inc.) operating in the noncontact mode. An aliquot of the sample at 20 μM protein concentration, after 25-fold dilution into 50 mM glycine buffer (pH 2.7), was applied onto a freshly cleaved mica plate. After incubation for 1 min, the mica surface was rinsed with 0.22 μm filtered water at pH 2.7. The mica was dried under vacuum for 45 min and was then scanned. The diameters (determined from the *Z*-heights in AFM images) and widths of the protofibrils were determined using the profile option in the program WSXM (*45*). The determination of each height distribution involved measurements on 150−200 individual protofibrils. The height of each individual protofibril was determined as the mean of the heights determined along its length.

Fourier-Transform Infrared (FTIR) Spectroscopy. FTIR measurements were carried out using a Thermo Nicholet-6700 FT-IR spectrometer (Thermo Scientific) equipped with a liquid nitrogen-cooled MCT detector. Buffers (see above) made in H_2O were used. The spectrometer was purged with ultrapure nitrogen gas. The solutions of protofibrils were concentrated ~50-fold using a Centricon (Millipore Corp.) of 10 kDa cutoff. The concentrated protofibrils were spun at 13000*g* for 10 min, the supernatant was applied onto a diamond crystal, and spectra were recorded in attenuated total reflectance (ATR) mode at a resolution of 4 cm^{-1}. Before each of the sample acquisitions, the buffer spectrum was recorded under the identical conditions and was used as blank. For each sample, 1024 scans were averaged.

Protein was seen to precipitate during the process of concentration in the case of the TFE-induced reaction. In the case of heat-induced reaction, no precipitation was observed. It was necessary to characterize the protein aggregates remaining in solution after concentrating the protein as well to characterize the protein precipitate formed during concentrating the TFE-induced protofibrils. For both the TFE-induced and heat-induced reactions, AFM imaging showed that the concentrated solutions, which were used for the acquisition of FTIR spectra (see above), contained protofibrils that were indistinguishable from the protofibrils before concentrating the solution (data not shown). Furthermore, the far-UV CD spectra of the two solutions showed the same difference in the positions of minima (data not shown) as seen in Figure 2C. The AFM images of the protein precipitate formed in the case of TFE-induced protofibrils showed only amorphous-type aggregates, possibly clumps of protofibrils; no further elongation was seen (data not shown).

Disaggregation of the Protofibrils at pH 8. Twenty micromolar protein solution (after completion of the aggregation reaction) was diluted 10-fold into ThT-containing 50 mM Tris buffer, so that the final solution was at pH 8 and contained 2 μM protein and 10 μM ThT. The decrease in the ThT-binding ability of the solution was then monitored continuously on a Fluoromax-3 spectrofluorometer (Jobin Yvon). The instrumental settings were the same as for the ThT binding assay.

Data Analysis. For each of the kinetic traces, the value of the signal at $t = 0$ as well as the amplitude of the signal change was determined by fitting the kinetic data points to the sigmoidal equation:

$$S = S_0 + \frac{S_\infty - S_0}{1 + e^{-((t - t_{50})/\tau)}} \quad (1)$$

where S_0 is the spectroscopic signal at $t = 0$, S_∞ is the final signal, t is the time, t_{50} is the time at which the change in signal is 50%, and τ is a characteristic time constant.

The value of the signal at $t = 0$ and the amplitude of the change in the signal determined from fitting the data to eq 1 were used to calculate the fractional change at each time point using the equation:

$$\text{fractional change} = \frac{S - S_0}{S_\infty - S_0} \quad (2)$$

The rate constant of elongation was then determined by fitting the kinetic data points, excluding those contributing to the initial ≤20% of the signal change, to the single exponential equation:

$$S = S_0 + a[1 - e^{-(t/\tau_{el})}] \quad (3)$$

where S_0 is the signal at $t = 0$, t is the time, a is the amplitude of the signal change, and τ_{el} represents the time constant of elongation.

RESULTS

TFE-Induced Protofibrils Differ from Heat-Induced Protofibrils in Their Structures. When TFE is added to a final concentration of 10% to the native state of barstar at pH 8, the far-UV CD spectrum does not change, and there is no increase in thioflavin T (ThT) binding ability (data not shown). This indicates that the protein remains native and does not aggregate upon the addition of TFE. In contrast, the addition of TFE to a final concentration of 10% to the A form of barstar at pH 2.7 alters the conformation of the A form (see below), which culminates in the formation of elongated, worm-like amyloid protofibrils (Figure 1A).

Figure 1 compares the AFM images of the amyloid protofibrils formed in the presence of 10% TFE at 25 °C (TFE-induced protofibrils) with those formed at 60 °C in the absence of TFE (heat-induced protofibrils). Both the TFE-induced and the heat-induced protofibrils appear as beaded curly structures in the AFM images (Figure 1A,B insets). The width of the TFE-induced protofibrils (20.5 ± 4.1 nm) appears to be significantly less than

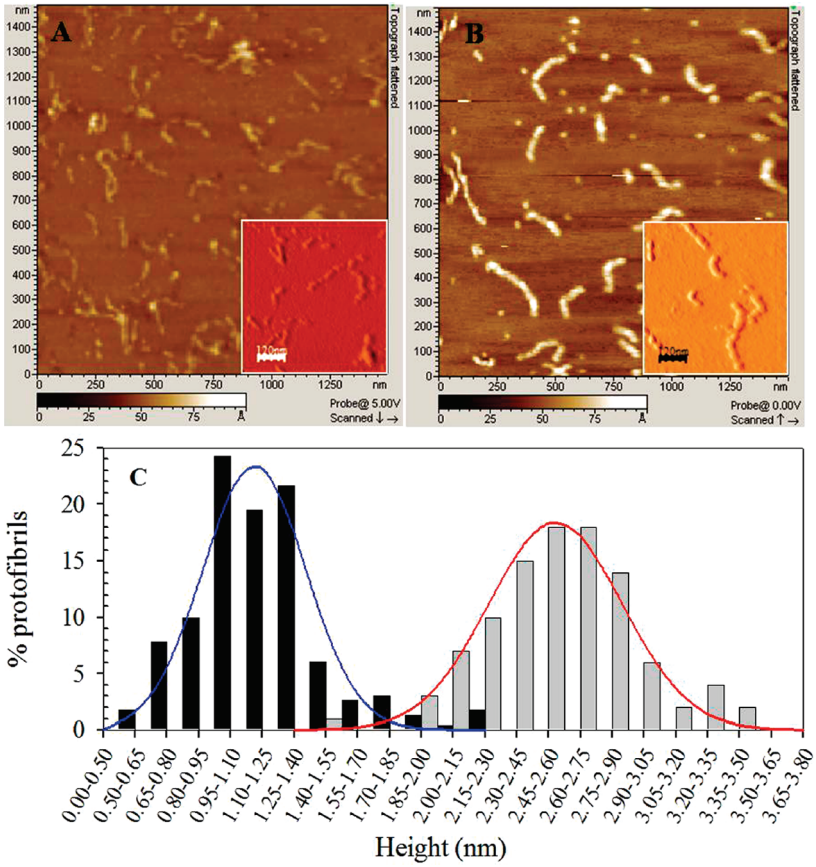

FIGURE 1: AFM images of TFE-induced and heat-induced protofibrils. (A) TFE-induced protofibrils. (B) Heat-induced protofibrils. The insets in panels A and B show magnified amplitude images to illustrate the beaded appearance of the protofibrils. The scale bars in the insets represent 120 nm. (C) Height distributions of the TFE-induced (black bars) and heat-induced (gray bars) protofibrils. The solid lines represent fits to a Gaussian equation.

that of the heat-induced protofibrils (31.1 ± 3.6 nm). Although absolute measurements of protofibril widths by AFM are prone to substantial errors arising from the finite width of the cantilever probe (which was the same for both measurements), the errors were minimized by measuring each width as the full width at half the maximum height. The measurement of height itself is more reliable, and the height, determined from the *Z*-height in the AFM images, is 1.14 ± 0.24 nm for the TFE-induced protofibrils, while it is 2.56 ± 0.32 nm for the protofibrils formed at 60 °C (Figure 1C). The heat-induced protofibrils formed at 40, 50, and 70 °C have the same heights and widths as those formed at 60 °C (data not shown).

The TFE-induced and heat-induced protofibrils also differ in their FTIR as well as far-UV CD spectra (Figure 2A−C). The FTIR spectra of the TFE-induced and heat-induced protofibrils (Figure 2A,B) are seen to differ in both the amide I (1600−1700 cm^{-1}) and the amide II (1500−1600 cm^{-1}) regions. In the amide I region, the TFE-induced protofibrils have a single peak at 1616 cm^{-1}. In contrast, the heat-induced protofibrils show two peaks in this region, one at 1621 cm^{-1} and another at 1650 cm^{-1}. In the amide II region, the TFE-induced protofibrils show a peak at ~1527 cm^{-1}, while the heat-induced protofibrils show a peak at ~1540 cm^{-1}.

The far-UV CD spectrum of the TFE-induced protofibrils is red shifted by ~3 nm as compared to that of the heat-induced protofibrils (Figure 2C). Moreover, the TFE-induced protofibrils have a significantly higher value of ellipticity at 216 nm (θ_{216nm}) than the heat-induced protofibrils. Furthermore, the TFE-induced protofibrils are much less stable than the heat-induced protofibrils (Figure 2D). Upon transfer to pH 8, the ThT binding ability disappears within 10 min for the TFE-induced protofibrils, while it takes ~60 h to disappear in the case of heat-induced protofibrils (*23*).

TFE-Induced Formation of Protofibrils Shows Distinct Kinetic Features. The observation that the TFE-induced and heat-induced protofibrils are structurally distinct suggests that the two growth conditions may result in different mechanisms of aggregation. To test this, four different structural probes were used to monitor the kinetics of protofibril formation under the two growth conditions. The probes used to monitor the kinetics included thioflavin T (ThT) fluorescence, ellipticity at 216 nm (θ_{216nm}), total scattering intensity (SI), and mean hydrodynamic radius (mean R_H). ThT fluorescence as well as θ_{216nm} probes conformational changes during aggregation, mean R_H reports on the growth (elongation) of the protein aggregates, and SI probes both the size and amount of aggregated materials.

Figure 3 shows the kinetics of the formation of TFE-induced as well as heat-induced protofibrils. In the case of the TFE-induced reaction, the kinetics measured with each of the probes are seen to be sigmoidal, with a lag phase, and are faster at 20 μM than at 5 μM protein concentration. Additionally, the θ_{216nm}-monitored kinetics shows a very fast initial (burst phase) change in the signal upon the addition of TFE to the A form (Figure 3B, E); thereafter, the signal changes in a sigmoidal manner. In contrast, the kinetics of heat-induced protofibril formation (Figure 3A−C insets) are seen to be monophasic without any lag phase, and single exponential fits to the kinetic data points extrapolate at $t = 0$ to the signal expected for the A form,

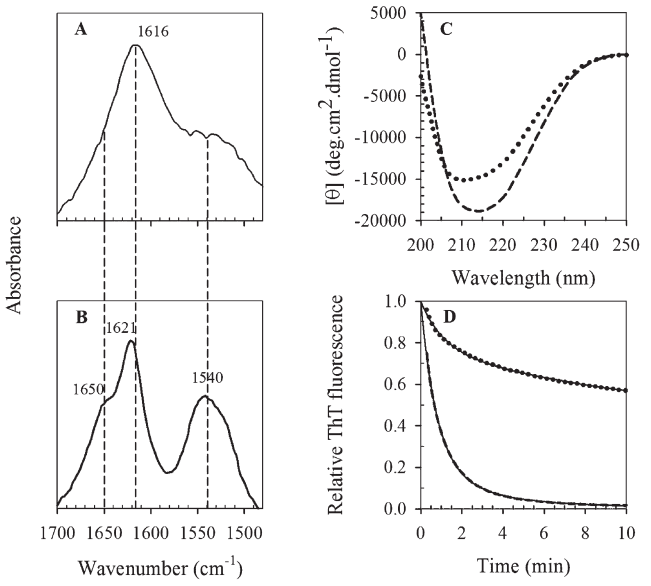

FIGURE 2: Structural characterization of TFE-induced and heat-induced protofibrils. (A) FTIR spectrum of TFE-induced protofibrils. (B) FTIR spectrum of heat-induced protofibrils. (C) Far-UV CD spectra of the TFE-induced (dashed line) and the heat-induced (dotted line) protofibrils. The initial monomer concentration was used to calculate the mean residual ellipticity, [θ]. (D) Kinetics of disaggregation, at pH 8, of the TFE-induced (dashed line) and the heat-induced (dotted line) protofibrils. The disaggregation kinetics was obtained by monitoring the decrease in the thioflavin T (ThT) fluorescence. The solid lines represent fits to a two-exponential equation. For each kinetic trace, the signal obtained at $t = 0$ by extrapolation of the fit was taken as 1.

suggesting that the A form acts as the direct precursor for the formation of protofibrils (*23*).

The high reproducibility of the experiments is evident from the small error in measurement at each of the time points. Importantly, identical kinetics were seen whether or not the sample aliquots were spun at 20000*g* for 2 min before the measurements of ThT fluorescence (data not shown). As suggested earlier (*25*), this observation indicates that no larger aggregates, which can interfere with the spectroscopic measurements, are formed.

Figure 4A shows the probe dependence of the elongation rate constant of TFE-induced protofibril formation. The elongation rate constants were determined by fitting the exponential increase phase (the data points corresponding to the initial 20% signal change were excluded) of the TFE-induced reaction to a single exponential equation. Figure 4B shows the probe dependence of the rate constant of heat-induced protofibril formation. The rate constants were determined from single exponential fits to the kinetic data points. For both the TFE- and the heat-induced reactions, the mean R_H-monitored kinetics are faster (~1.5-fold) than the kinetics monitored with ThT fluorescence and θ_{216nm}. For the heat-induced reaction, the SI-monitored kinetics are significantly (>2-fold) slower than the mean R_H-monitored kinetics. In contrast, the SI-monitored and mean R_H-monitored rate constants have similar values for the TFE-induced reaction.

Dependence of TFE-Induced Amyloid Protofibril Formation on Protein Concentration. The kinetics of TFE-induced protofibril formation were monitored in a range of protein concentrations. At each of the protein concentrations studied, and with each of the probes, the kinetics are well described as a sigmoidal process with an initial lag phase (Figure 5A–C). The rate constant of protofibril formation increases, and the lag time decreases with an increase in the initial protein concentration. In the θ_{216nm}-monitored kinetics, the fractional change associated with the burst phase is observed to be the same for all the protein concentrations studied (Figure 5B).

The dependence on protein concentration of the elongation rate constant, determined from the use of three probes, is shown in Figure 5D. The rate constant first increases with an increase in protein concentration and then saturates at a protein concentration of ~5–10 μM. This indicates, as in the case of the heat-induced reaction (*23*, *25*), that the rate-determining step at lower protein concentrations involves the association of protein molecules, while at higher protein concentrations the rate is limited by conformational change.

The lag time at each protein concentration was determined by extrapolation of the single exponential fit (to the exponential increase phase) to the time at which the change in the probe signal is zero. The lag time decreases with an increase in the protein concentration (Figure 5D inset), but its dependence on protein concentration is weak: the slope of a log(lag time) versus log (protein concentration) is only 0.34.

DISCUSSION

TFE-Induced and Heat-Induced Protofibrils Differ in Their Structures. It has been suggested that a bilayer (pair) of β-sheets, in which the side chains protruding from the two sheets intercalate to form a steric zipper, is the basic structural motif of amyloid fibrils (*5*). Such a bilayer is expected (*3*) to have a height of about 2.3 nm. The height of 2.56 ± 0.32 nm seen for the heat-induced protofibrils (Figure 1C) therefore suggests that they are formed as a bilayer of β-sheets (Figure 6). On the other hand, the height of 1.14 ± 0.24 nm observed for the TFE-induced protofibrils suggests that they are formed as a β-sheet monolayer. A β-sheet monolayer is expected to have a thickness between 1 and 1.7 nm, depending on the extent to which different side chains protrude on either side of the main chain, and indeed, the single β-sheet in native barstar has a thickness of 1.03 ± 0.24 nm. It seems therefore that the TFE-induced protofibrils consist of a monolayer β-sheet structure (Figure 6) formed by the alignment of the β-strands contributed by different protein molecules and which elongates in the direction of the axis of the protofibril. The different widths observed for TFE-induced and heat-induced protofibrils in the AFM images suggest that they differ also in the lengths of the β-strands that align to form the β-sheet.

Several other results support the interpretation of the AFM experiments that the TFE-induced protofibrils form a β-sheet monolayer, while the heat-induced protofibrils form a β-sheet bilayer. Multistranded protofibrils, as would be those built from a bilayer β-sheet motif, are expected (*46*) to be much more stable than single-stranded protofibrils, as would be those built from a monolayer β-sheet motif. The observation that TFE-induced protofibrils are far less stable than heat-induced protofibrils, to a change in pH from 2.7 to 8 (Figure 2D), suggests that the former is single stranded if the latter is double stranded. In the case of heat-induced formation of protofibrils, the observation that the mean R_H-monitored kinetics are significantly faster than the kinetics monitored by SI (Figure 4B) had suggested (*23*) that elongated protofibrils associate laterally to form mature multistranded protofibrils, because such lateral association would lead to an increase in scattering intensity without an apparent increase in the mean R_H (*47*). On the other hand, in the case of TFE-induced formation of protofibrils, the mean R_H-monitored and

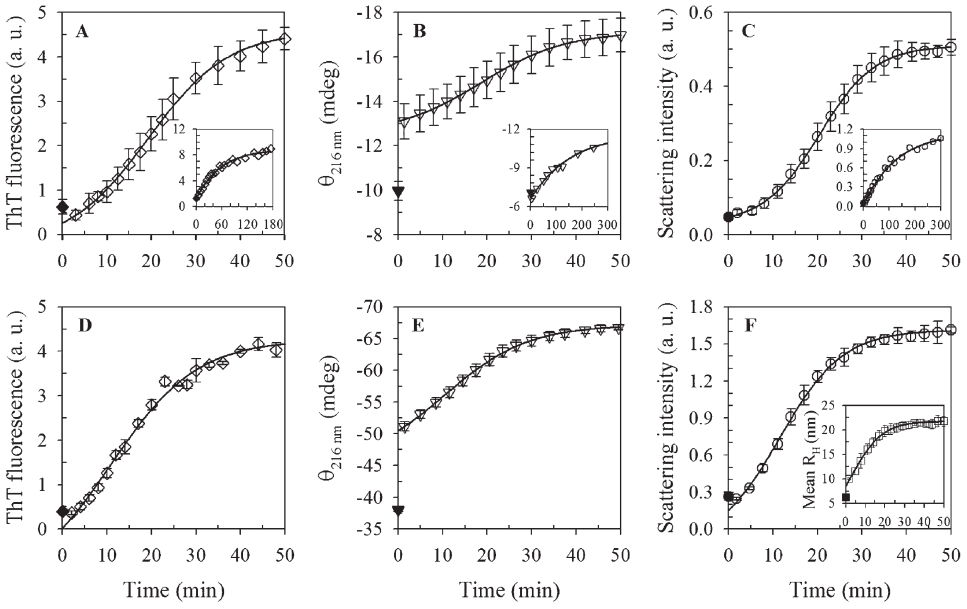

FIGURE 3: Kinetics of TFE-induced and heat-induced amyloid protofibril formation at 5 and 20 μM protein concentrations. In the case of the TFE-induced reaction, the protein was incubated with 10% TFE at pH 2.7, 25 °C. The heat-induced formation of protofibrils was carried out at 60 °C, pH 2.7, in the absence of TFE. Panels A−C show the kinetics monitored by thioflavin T (ThT) fluorescence, ellipticity at 216 nm (θ_{216nm}), and scattering intensity (SI), respectively, at 5 μM protein concentration. The data shown in the insets in panels A−C are representative kinetic curves for the corresponding heat-induced reactions and are taken from ref (*23*). Panels D−F show the TFE-induced kinetic traces monitored by ThT fluorescence, θ_{216nm}, and SI, respectively, at 20 μM protein concentration. The inset in panel F shows the mean R_H-monitored kinetics of TFE-induced protofibril formation at 20 μM protein concentration. In all of the panels, the filled symbols represent the signal of the A form, and the open symbols represent the kinetic data points. The error bars represent either the standard deviations obtained from three independent experiments or the spreads in the signals determined from two independent experiments. In panels A−F as well as in the inset in panel F, the solid lines are fits to a sigmoidal equation (eq 1). In the insets in panels A−C, the solid lines are fits to a single exponential equation (eq 3).

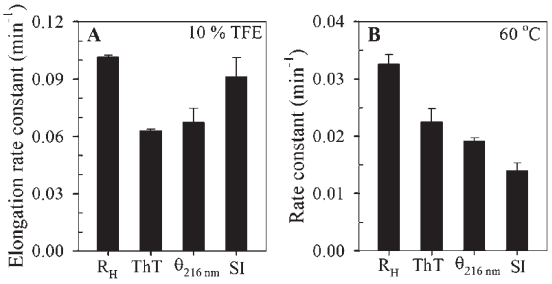

FIGURE 4: Probe dependence of the observed rate constants. Aggregation reactions at 20 μM protein concentration were monitored using mean hydrodynamic radius (R_H), thioflavin T fluorescence (ThT), ellipticity at 216 nm (θ_{216nm}), and scattering intensity (SI) as the probes. In the case of the TFE-induced reaction (A), the protein was incubated with 10% TFE at pH 2.7, 25 °C. The heat-induced formation of protofibrils (B) was carried out at 60 °C, pH 2.7. The error bars represent either the standard deviations obtained from three separate experiments or the spread in the values obtained from two independent experiments.

SI-monitored rate constants are similar (Figure 4A), which suggests that no lateral association of the elongated protofibrils occurs and that the TFE-induced protofibrils are therefore single stranded.

TFE-Induced and Heat-Induced Protofibrils Differ in Their Internal Structures. The FTIR spectra of the TFE-induced protofibrils differ significantly from those of the heat-induced protofibrils (Figure 2A,B), suggesting that they also differ in their secondary structures. The presence of a peak in the 1615−1643 cm^{-1} region (*48*, *49*) suggests that both the TFE-induced and the heat-induced protofibrils contain amyloid-like β-sheet structures. The observation that the position of this peak in the TFE-induced protofibrils (1616 cm^{-1}) differs by 5 cm^{-1} from that in the heat-induced protofibrils (1621 cm^{-1}) suggests that the β-sheets in the two differently generated protofibrils differ in their internal structures. Furthermore, the presence of a peak at 1650 cm^{-1} in the case of heat-induced protofibrils suggests that they are not pure β-sheet structures but that other structures (*48*, *50*) (helices and/or random coils) are also present. In contrast, the peak at 1650 cm^{-1} is absent in the case of TFE-induced protofibrils, suggesting that they contain relatively more β-sheet structures and less of other structures, if any.

The far-UV CD spectra of the TFE-induced and heat-induced protofibrils differ in the position of the minima as well as in the values of mean residual ellipticity (Figure 2C). The far-UV CD spectrum of the heat-induced protofibrils shows a minimum at ~211 nm, while that of the TFE-induced protofibrils shows a minimum at ~214 nm and a higher value of mean residual ellipticity. This suggests, as do the FTIR spectra, that the heat-induced protofibrils are not pure β-sheets but that they also possess other secondary structures, while the TFE-induced protofibrils possess more β-sheet structures and less of other secondary structures, if any. The non-β-sheet structures present in the heat-induced protofibrils might be responsible for their height being marginally more than that expected for a pure β-sheet bilayer (see above).

Being multistranded, the heat-induced protofibrils scatter light more than the apparently single-stranded TFE-induced protofibrils (Figure 3C and inset). Light scattering by large protein aggregates is known to cause a red shift in the far-UV CD spectrum (*51*). The observation that the far-UV CD spectrum of the heat-induced protofibrils shows a minimum that is, instead, blue shifted by ~3 nm compared to that seen for the TFE-induced protofibrils (Figure 2C) suggests that the difference in the far-UV CD spectra of the protofibrils formed under the two

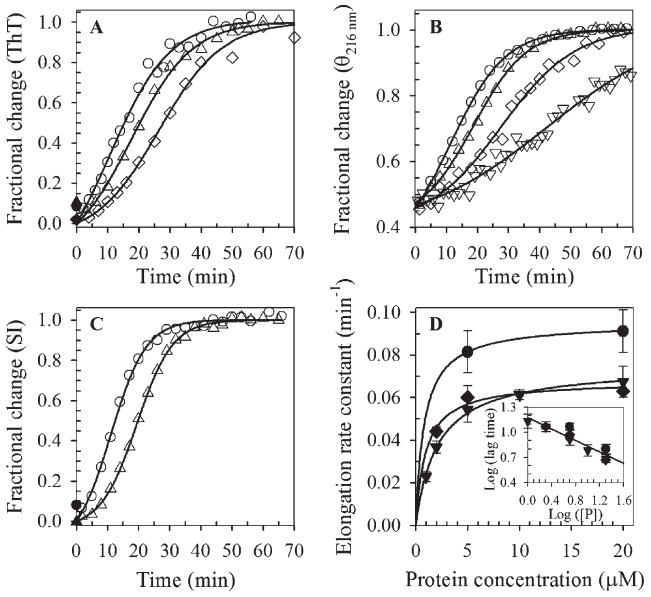

FIGURE 5: Protein concentration dependence of the kinetics of TFE-induced amyloid protofibril formation. The reaction was carried out at 10% TFE concentration, at pH 2.7, 25 °C. The concentrations of protein used were 1 μM (▽), 2 μM (◇), 5 μM (△), and 20 μM (○). (A) Thioflavin T (ThT) fluorescence-monitored kinetics. (B) Ellipticity at 216 nm- (θ_{216nm}-) monitored kinetics. (C) Scattering intensity- (SI-) monitored kinetics. In panels A−C, filled symbols represent the signals of the A form, and the kinetic data points are represented by the open symbols. In panels A and C, both the $t = 0$ signal and the amplitude of the change in the signal, used to calculate the fractional change, were obtained from a fit of the kinetic data points to eq 1. In panel B, the signal of the A form was taken as the $t = 0$ signal, and the amplitude of the signal change was obtained by subtracting the signal of the A form from the final signal obtained from the fit to the kinetic data points to eq 1. In panels A−C, the solid lines are fits to eq 1. (D) Dependence of the elongation rate constants on protein concentration. The solid lines have been drawn by inspection only. The inset in panel D is a plot of log(lag time) versus log(protein concentration). The initial monomer concentration was used. The solid line is a linear fit common to all of the data points obtained from using the three probes. In panel D and the inset therein, the values obtained from ThT fluorescence-, θ_{216nm}-, and SI-monitored kinetics are represented by ◆, ▼, and ●, respectively.

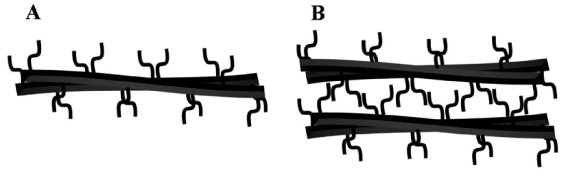

FIGURE 6: Models of amyloid protofibrils. (A) Cartoon representation of the TFE-induced protofibrils. (B) Cartoon representation of the heat-induced protofibrils.

different growth conditions is not an artifact due to light scattering. Instead, the difference points to structural differences in the protofibrils formed under the two different growth conditions.

Mechanism of Formation of TFE-Induced Protofibrils. From previous studies (*22*, *23*, *25*) of heat-induced protofibril formation, it is known that the A form first grows progressively in size into higher oligomeric intermediates (HOIs). The HOIs appear as spherical oligomers in AFM images, and they further assemble into the beaded, worm-like protofibrils. No lag phase is seen (*23*, *25*), protofibril formation is the fastest at the start of the reaction, and the extent of protofibril formation increases exponentially with time to a finite limiting value. Heat-induced protofibril formation appears therefore to follow the isodesmic (linear) mechanism (*52*), in which the affinity of the protofibril for its building blocks (the HOIs) is independent of protofibril length. In contrast, TFE-induced protofibril formation appears to be cooperative, with a lag phase followed by an elongation phase.

TFE-induced protofibril formation shows two of the three defining features of a nucleation-dependent polymerization (NDP) mechanism (*52*, *53*): a lag phase is seen (Figure 3), and seeding reduces the lag time (Supporting Information Figure S1). But the lag phase has a weak dependence on protein concentration (Figure 5D inset), and seeding has only a weak effect on the aggregation kinetics (Supporting Information Figure S1). The third defining criterion of the NDP mechanism, namely, the observation of a critical concentration below which elongation does not occur, is not at all met: a plot of either the amplitude (data not shown) or the elongation rate constant (Figure 5D) of the θ_{216nm}-monitored aggregation reaction versus protein concentration does not intercept the *x*-axis at a nonzero value. Hence, TFE-induced protofibril formation cannot be described by an NDP mechanism. On the other hand, the lag phase observed in TFE-induced protofibril formation can also be explained on the basis of an isodesmic mechanism (*53*). It appears that TFE-induced protofibril formation might have features of both the NDP and isodesmic mechanisms. There could be multiple steps, and the affinity of the protofibril for its building blocks might change for each step.

The Pathways of Formation of TFE-Induced and Heat-Induced Protofibrils Are Different. The kinetics of TFE-induced protofibril formation, as monitored by four different structural probes (Figure 3), do indeed indicate that the A form transforms into protofibrils in multiple steps. The burst phase evident in the θ_{216nm}-monitored kinetics (Figure 3B,E) suggests that, immediately upon the addition of TFE, the A form equilibrates with an alternative conformation, the A_α form, which is much more α-helical than the A form (Supporting Information Figure S2A). If the A and A_α forms are both present at equilibrium, either could be on the direct pathway of protofibril formation. Alternatively, the A form could be completely converted into the A_α form, which, in turn, acts as the precursor for the formation of protofibrils. In fact, the latter possibility seems more likely, since the far-UV CD spectra, at ~2.5 min after the addition of TFE up to different final concentrations ranging from 0 to 20%, do not show a clear isodichroic point (Supporting Information Figure S2B,C), which is expected if the A form exists in a two-state equilibrium with the A_α form (*54*, *55*). Importantly, the observation that the fractional burst phase change is independent of protein concentration (Figure 5B) suggests that, at each protein concentration, the addition of TFE leads to the conversion of all the protein molecules into the A_α form. For amyloid-β protein, too, accumulation of an α-helical species is seen during the process of aggregation (*56*, *57*). Moreover, the kinetics of aggregation of the amyloid-β protein are seen to be affected by the extent of α-helix stabilization by TFE (*39*).

Hence, unlike the heat-induced reaction, wherein the A form acts as the direct precursor (*22*, *23*) (see above), the TFE-induced formation of amyloid protofibrils seems to commence from the structurally distinct A_α form (see above). TFE-induced formation of amyloid protofibrils therefore involves a pathway that is different from that of heat-induced formation (*23*) of protofibrils. The former pathway also does not appear to involve a lateral

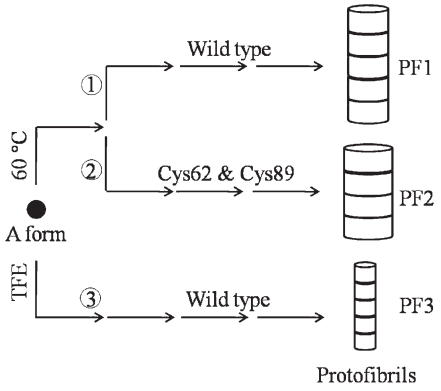

FIGURE 7: Polymorphism in amyloid protofibrils. The amyloid protofibrils formed at 60 °C by wild-type barstar (PF1) differ from those formed, under the same conditions, by two single cysteine-containing variants of barstar (PF2) (*25*). The amyloid protofibrils formed in the presence of 10% TFE, at 25 °C (PF3), are distinct from the former two. These three structural polymorphs of amyloid protofibrils formed by barstar differ in their diameters, as determined from the *Z*-heights in AFM images, as well as in their structures.

association step, as does the latter pathway (see above). Not surprisingly, the TFE-induced reaction leads to the formation of protofibrils that are structurally distinct from the heat-induced protofibrils (Figures 1 and 2).

At the end of the lag phase of TFE-induced protofibril formation, dynamic light scattering data indicate that the A_α form has transformed into a larger but heterogeneous intermediate, the I_L oligomer (data not shown). The far-UV CD spectrum of the I_L oligomer indicates that it has slightly more secondary structure than that of the A_α form, but the pronounced minimum at 214 nm, characteristic of conversion to β-sheet structure, is not seen (data not shown). The observation that the probe dependence (when monitored with ThT fluorescence, θ_{216nm}, and mean RH) of the elongation rate constant of TFE-induced protofibril formation is similar to that of the rate constant of heat-induced protofibril formation (Figure 4) suggests that, as in the case of the heat-induced reaction (*23*), the conformational conversion to β-sheet structure during the transformation of I_L oligomers into protofibrils occurs either after or concurrently with the elongation.

Pathway Heterogeneity Underlies the Structural Polymorphism of Amyloid Protofibrils. Previous studies on the heat-induced formation of protofibrils by wild-type barstar (*23*) as well as by a set of single cysteine-containing variants of the protein (*25*) have suggested that there exist alternative pathways for the formation of heat-induced amyloid protofibrils. Interestingly, the amyloid protofibrils formed on the alternative pathways appeared to be structurally distinct. The oligomeric intermediates, which preceded the formation of protofibrils on the aggregation pathway, were also found to be structurally distinct (*25*). This report on TFE-induced protofibril formation shows that a change in the growth conditions can also lead to the utilization of a separate aggregation pathway and, thereby, can lead to the formation of amyloid protofibrils of distinct internal structures and of distinct external dimensions (Figure 7).

The formation of structurally distinct mature amyloid fibrils by the same protein, in response to a change in amino acid sequence or growth conditions, has been reported earlier for other proteins (*6*−*10*, *13*). The results reported here for barstar indicate that amyloid protofibrils formed by the same protein too can show structural polymorphism and that the structural polymorphs arise due to different pathways being followed for their formation. The structural polymorphism seen in amyloid protofibrils might explain the heterogeneity seen in mature amyloid fibrils and thus may provide an insight into the origin of prion strain diversity (*58*). The existence of alternative pathways for the formation of amyloid protofibrils, together with information on switching among the available pathways, which thereby generates different amyloid conformations, is of significance for the formulation of therapies against amyloid-related disorders (*59*), as well as for the development of amyloid-based nanomaterials (*60*).

ACKNOWLEDGMENT

We thank members of our laboratory for discussion and comments on the manuscript. The AFM images were collected at the Central Imaging Facility of NCBS.

SUPPORTING INFORMATION AVAILABLE

The effect of seeding on TFE-induced amyloid protofibril formation and the effect of adding TFE on the far-UV CD spectrum of the A form. This material is available free of charge via the Internet at http://pubs.acs.org.

REFERENCES

1. Chiti, F., and Dobson, C. M. (2006) Protein misfolding, functional amyloid, and human disease. *Annu. Rev. Biochem. 75*, 333–366.
2. Sunde, M., Serpell, L. C., Bartlam, M., Fraser, P. E., Pepys, M. B., and Blake, C. C. F. (1997) Common core structure of amyloid fibrils by synchrotron X-ray diffraction. *J. Mol. Biol. 273*, 729–739.
3. Nelson, R., Sawaya, M. R., Balbirnie, M., Madsen, A. Ø., Riekel, C., Grothe, R., and Eisenberg, D. (2005) Structure of the cross-β spine of amyloid-like fibrils. *Nature 435*, 773–778.
4. O'Nuallain, B., and Wetzel, R. (2002) Conformational Abs recognizing a generic amyloid fibril epitope. *Proc. Natl. Acad. Sci. U.S.A. 99*, 1485–1490.
5. Sawaya, M. R., Sambashivan, S., Nelson, R., Ivanova, M. I., Sievers, S. A., Apostol, M. I., Thompson, M. J., Balbirnie, M., Wiltzius, J. J. W., McFarlane, H. T., Madsen, A. Ø., Riekel, C., and Eisenberg, D. (2007) Atomic structures of amyloid cross-β spines reveal varied steric zippers. *Nature 447*, 453–457.
6. Petkova, A. T., Leapman, R. D., Guo, Z., Yau, W., Mattson, M. P., and Tycko, R. (2005) Self-propagating, molecular-level polymorphism in Alzheimer's β-amyloid fibrils. *Science 307*, 262–265.
7. Kad, N. M., Thomson, N. H., Smith, D. P., Smith, D. A., and Radford, S. E. (2001) β_2-microglobulin and its deamidated variant, N17D form amyloid fibrils with a range of morphologies in vitro. *J. Mol. Biol. 313*, 559–571.
8. Gosal, W. S., Morten, I. J., Hewitt, E. W., Smith, D. A., Thomson, N. H., and Radford, S. E. (2005) Competing pathways determine fibril morphology in the self-assembly of β_2-microglobulin into amyloid. *J. Mol. Biol. 351*, 850–864.
9. Hess, S., Lindquist, S. L., and Scheibel, T. (2007) Alternative assembly pathways of the amyloidogenic yeast prion determinant Sup35−NM. *EMBO Rep. 8*, 1196–1201.
10. Goldsbury, C., Frey, P., Olivieri, V., Aebi, U., and Muller, S. A. (2005) Multiple assembly pathways underlie amyloid-β fibril polymorphisms. *J. Mol. Biol. 352*, 282–298.
11. Kad, N. M., Myers, S. L., Smith, D. P., Smith, D. A., Radford, S. E., and Thomson, N. H. (2003) Hierarchical assembly of β_2-microglobulin amyloid *in vitro* revealed by atomic force microscopy. *J. Mol. Biol. 330*, 785–797.
12. Serpell, L. C., Blake, C. C. F., and Fraser, P. E. (2000) Molecular structure of a fibrillar Alzheimer's Aβ fragment. *Biochemistry 39*, 13269–13275.
13. Heise, H., Hoyer, W., Becker, S., Andronesi, O. C., Riedel, D., and Baldus, M. (2005) Molecular-level secondary structure, polymorphism, and dynamics of full-length α-synuclein fibrils studied by solid-state NMR. *Proc. Natl. Acad. Sci. U.S.A. 102*, 15871–15876.
14. Ferrone, F. (1999) Analysis of protein aggregation kinetics. *Methods Enzymol. 309*, 256–274.

15. Collins, S. R., Douglass, A., Vale, R. D., and Weissman, J. S. (2004) Mechanism of prion propagation: amyloid growth occurs by monomer addition. *PLoS Biol. 2* (e321), 1582–1590.
16. Smith, A. M., Jahn, T. R., Ashcroft, A. E., and Radford, S. E. (2006) Direct observation of oligomeric species formed in the early stages of amyloid fibril formation using electrospray ionisation mass spectrometry. *J. Mol. Biol. 364*, 9–19.
17. Serio, T. R., Cashikar, A. G., Kowal, A. S., Sawicki, G. J., Moslehi, J. J., Serpell, L., Arnsdorf, M. F., and Lindquist, S. L. (2000) Nucleated conformational conversion and the replication of conformational information by a prion determinant. *Science 289*, 1317–1321.
18. Bitan, G., Kirkitadze, M. D., Lomakin, A., Vollers, S. S., Benedek, G. B., and Teplow, D. B. (2003) Amyloid β-protein (Aβ) assembly: Aβ40 and Aβ42 oligomerize through distinct pathways. *Proc. Natl. Acad. Sci. U.S.A. 100*, 330–335.
19. Modler, A. J., Gast, K., Lutsch, G., and Damaschun, G. (2003) Assembly of amyloid protofibrils *via* critical oligomers—a novel pathway of amyloid formation. *J. Mol. Biol. 325*, 135–148.
20. Hurshman, A. R., White, J. T., Powers, E. T., and Kelly, J. W. (2004) Transthyretin aggregation under partially denaturing conditions is a downhill polymerization. *Biochemistry 43*, 7365–7381.
21. Carrotta, R., Manno, M., Bulone, D., Martorana, V., and Biagio, P. L. S. (2005) Protofibril formation of amyloid β-protein at low pH via a non-cooperative elongation mechanism. *J. Biol. Chem. 280*, 30001–30008.
22. Mukhopadhyay, S., Nayak, P. K., Udgaonkar, J. B., and Krishnamoorthy, G. (2006) Characterization of the formation of amyloid protofibrils from barstar by mapping residue-specific fluorescence dynamics. *J. Mol. Biol. 358*, 935–942.
23. Kumar, S., Mohanty, S. K., and Udgaonkar, J. B. (2007) Mechanism of formation of amyloid protofibrils of barstar from soluble oligomers: evidence for multiple steps and lateral association coupled to conformational conversion. *J. Mol. Biol. 367*, 1186–1204.
24. Jain, S., and Udgaonkar, J. B. (2008) Evidence for stepwise formation of amyloid fibrils by the mouse prion protein. *J. Mol. Biol. 382*, 1228–1241.
25. Kumar, S., and Udgaonkar, J. B. (2009) Conformational conversion may precede or follow aggregate elongation on alternative pathways of amyloid protofibril formation. *J. Mol. Biol. 385*, 1266–1276.
26. Kheterpal, I., Chen, M., Cook, K. D., and Wetzel, R. (2006) Structural differences in Aβ amyloid protofibrils and fibrils mapped by hydrogen exchange−mass spectrometry with on-line proteolytic fragmentation. *J. Mol. Biol. 361*, 785–795.
27. Kodali, R., and Wetzel, R. (2007) Polymorphism in the intermediates and products of amyloid assembly. *Curr. Opin. Struct. Biol. 17*, 48–57.
28. Surewicz, W. K., Jones, E. M., and Apetri, A. C. (2006) The emerging principles of mammalian prion propagation and transmissibility barriers: insight from studies in vitro. *Acc. Chem. Res. 39*, 654–662.
29. DePace, A. H., and Weissman, J. S. (2002) Origins and kinetic consequences of diversity in Sup35 yeast prion fibers. *Nat. Struct. Mol. Biol. 9*, 389–396.
30. Chien, P., DePace, A. H., Collins, S. R., and Weissman, J. S. (2003) Generation of prion transmission barriers by mutational control of amyloid conformations. *Nature 424*, 948–951.
31. Tanaka, M., Chien, P., Naber, N., Cooke, R., and Weissman, J. S. (2004) Conformational variations in an infectious protein determine prion strain differences. *Nature 428*, 323–328.
32. Khurana, R., and Udgaonkar, J. B. (1994) Equilibrium unfolding studies of barstar: evidence for an alternative conformation which resembles a molten globule. *Biochemistry 33*, 106–115.
33. Swaminathan, R., Periasamy, N., Udgaonkar, J. B., and Krishnamoorthy, G. (1994) Molten globule-like conformation of barstar: a study by fluorescence dynamics. *J. Phys. Chem. 98*, 9270–9278.
34. Juneja, J., Bhavesh, N. S., Udgaonkar, J. B., and Hosur, R. V. (2002) NMR identification and characterization of the flexible regions in the 160 kDa molten globule-like aggregate of barstar at low pH. *Biochemistry 41*, 9885–9899.
35. Gast, K., Modler, A. J., Damaschun, H., Kröber, R., Lutsch, G., Zirwer, D., Golbik, R., and Damaschun, G. (2003) Effect of environmental conditions on aggregation and fibril formation of barstar. *Eur. Biophys. J. 32*, 710–723.
36. Munishkina, L. A., Phelan, C., Uversky, V. N., and Fink, A. L. (2003) Conformational behavior and aggregation of α-synuclein in organic solvents: modeling the effects of membranes. *Biochemistry 42*, 2720–2730.
37. Chiti, F., Webster, P., Taddei, N., Clark, A., Stefani, M., Ramponi, G., and Dobson, C. M. (1999) Designing conditions for *in vitro* formation of amyloid protofilaments and fibrils. *Proc. Natl. Acad. Sci. U.S.A. 96*, 3590–3594.
38. Bucciantini, M., Giannoni, E., Chiti, F., Baroni, F., Formigli, L., Zurdo, J., Taddei, N., Ramponi, G., Dobson, C. M., and Stefani, M. (2002) Inherent toxicity of aggregates implies a common mechanism for protein misfolding diseases. *Nature 416*, 507–511.
39. Fezoui, Y., and Teplow, D. B. (2002) Kinetic studies of amyloid β-protein fibril assembly: differential effects of α-helix stabilization. *J. Biol. Chem. 277*, 36948–36954.
40. Yamaguchi, K., Naiki, H., and Goto, Y. (2006) Mechanism by which the amyloid-like fibrils of a β2-microglobulin fragment are induced by fluorine-substituted alcohols. *J. Mol. Biol. 363*, 279–288.
41. Rajan, R., and Balaram, P. (1996) A model for interaction of trifluoroethanol with peptides and proteins. *Int. J. Pept. Protein Res. 48*, 328–336.
42. Buck, M. (1998) Trifuoroethanol and colleagues: cosolvents come of age. Recent studies with peptides and proteins. *Q. Rev. Biophys. 31*, 297–355.
43. Nichols, M. R., Moss, M. A., Reed, D. K., Cratic-McDaniel, S., Hoh, J. H., and Rosenberry, T. L. (2005) Amyloid-β protofibrils differ from amyloid-β aggregates induced in dilute hexafluoroisopropanol in stability and morphology. *J. Biol. Chem. 280*, 2471–2480.
44. Nichols, M. R., Moss, M. A., Reed, D. K., Hoh, J. H., and Rosenberry, T. L. (2005) Amyloid-β aggregates formed at polar-nonpolar interfaces differ from amyloid-β protofibrils produced in aqueous buffers. *Microsc. Res. Tech. 67*, 164–174.
45. Horcas, I., Fernández, R., Gómez-Rodríguez, J. M., Colchero, J., Gómez-Herrero, J., and Baro, A. M. (2007) WSXM: a software for scanning probe microscopy and a tool for nanotechnology. *Rev. Sci. Instrum. 78*, 013705.
46. Howard, J. (2001) Polymerization of cytoskeletal filaments, in Mechanics of motor proteins and the cytoskeleton, p 155, Sinauer Associates, Sunderland, MA.
47. Lomakin, A., Benedek, G. B., and Teplow, D. B. (1999) Monitoring protein assembly using quasielastic light scattering microscopy. *Methods Enzymol. 309*, 429–459.
48. Seshadri, S., Khurana, R., and Fink, A. L. (1999) Fourier transform infrared spectroscopy in analysis of protein deposits. *Methods Enzymol. 309*, 559–576.
49. Zandomeneghi, G., Krebs, M. R. H., Mccammon, M. G., and Fändrich, M. (2004) FTIR reveals structural differences between native β-sheet proteins and amyloid fibrils. *Protein Sci. 13*, 3314–3321.
50. Susi, H. (1972) Infrared spectroscopy—conformation. *Methods Enzymol. 26*, 455–472.
51. Soldi, G., Bemporad, F., Torrassa, S., Relini, A., Ramazzotti, M., Taddei, N., and Chiti, F. (2005) Amyloid formation of a protein in the absence of initial unfolding and destabilization of the native state. *Biophys. J. 89*, 4234–4244.
52. Oosawa, F., and Kasai, M. (1962) A theory of linear and helical aggregations of macromolecules. *J. Mol. Biol. 4*, 10–21.
53. Frieden, C. (2007) Protein aggregation processes: in search of the mechanism. *Protein Sci. 16*, 2334–2344.
54. Woody, R. W. (1995) Circular dichroism. *Methods Enzymol. 246*, 34–71.
55. Vidal, P., Morris, M. C., Chaloin, L., Méry, J., Heitz, F., and Divita, G. (1997) Conformations of a synthetic peptide which facilitates the cellular delivery of nucleic acids. *Lett. Pept. Sci. 4*, 227–230.
56. Walsh, D. M., Hartley, D. M., Kusumoto, Y., Fezoui, Y., Condron, M. M., Lomakin, A., Benedek, G. B., Selkoe, D. J., and Teplow, D. B. (1999) Amyloid β-protein fibrillogenesis: structure and biological activity of protofibrillar intermediates. *J. Biol. Chem. 274*, 25945–25952.
57. Kirkitadze, M. D., Condron, M. M., and Teplow, D. B. (2001) Identification and characterization of key kinetic intermediates in amyloid β-protein fibrillogenesis. *J. Mol. Biol. 312*, 1103–1119.
58. Eghiaian, F., Daubenfeld, T., Quenet, Y., Audenhaege, M. V., Bouin, A., Rest, G. V. D., Grosclaude, J., and Rezaei, H. (2007) Diversity in prion protein oligomerization pathways results from domain expansion as revealed by hydrogen/deuterium exchange and disulfide linkage. *Proc. Natl. Acad. Sci. U.S.A. 104*, 7414–7419.
59. Sciarretta, K. L., Gordon, D. J., and Meredith, S. C. (2006) Peptide-based inhibitors of amyloid assembly. *Methods Enzymol. 413*, 273–312.
60. Hamada, D., Yanagihara, I., and Tsumoto, K. (2004) Engineering amyloidogenicity towards the development of nanofibrillar materials. *Trends Biotechnol. 22*, 93–97.